

Direct Electrical Neurostimulation with Organic Pigment Photocapacitors

David Rand, Marie Jakešová, Gur Lubin, Ieva Vėbraitė, Moshe David-Pur, Vedran Đerek, Tobias Cramer, Niyazi Serdar Sariciftci, Yael Hanein,* and Eric Daniel Głowacki*

Dedicated to Professor Ching Tang on occasion of his 70th birthday

An efficient nanoscale semiconducting optoelectronic system is reported, which is optimized for neuronal stimulation: the organic electrolytic photocapacitor. The devices comprise a thin (80 nm) trilayer of metal and p–n semiconducting organic nanocrystals. When illuminated in physiological solution, these metal–semiconductor devices charge up, transducing light pulses into localized displacement currents that are strong enough to electrically stimulate neurons with safe light intensities. The devices are freestanding, requiring no wiring or external bias, and are stable in physiological conditions. The semiconductor layers are made using ubiquitous and nontoxic commercial pigments via simple and scalable deposition techniques. It is described how, in physiological media, photovoltage and charging behavior depend on device geometry. To test cell viability and capability of neural stimulation, photostimulation of primary neurons cultured for three weeks on photocapacitor films is shown. Finally, the efficacy of the device is demonstrated by achieving direct optoelectronic stimulation of light-insensitive retinas, proving the potential of this device platform for retinal implant technologies and for stimulation of electrogenic tissues in general. These results substantiate the conclusion that these devices are the first non-Si optoelectronic platform capable of sufficiently large photovoltages and displacement currents to enable true capacitive stimulation of excitable cells.

devices in recent decades. Eliminating the need for wiring, optical stimulation is an alternative approach, which is inherently less invasive than electrodes.^[7] The motivation to achieve wireless access to electrophysiological processes has driven the field of optogenetics, involving genetic transfection of target cells with light-sensitive ion channels.^[8] Optogenetics is a relatively mature field, which showcases the high spatial and temporal resolution and minimal invasiveness afforded by light. Nevertheless, the reliance on genetic modification imposes many obstacles.

Nongenetic approaches to impart long-term photosensitivity to electrophysiological processes are highly desired for in vivo applications in humans, including peripheral or central nervous therapeutics, and implants such as retinal prostheses.^[9,10] Despite the clear need for nongenetic means to optically stimulate neurons, the range of available devices suitable to facilitate neuronal response under illumination is limited and silicon optoelectronics have been the primary platform in emerging

Stimulation of neurons in a localized and safe manner is important both as an investigative tool and as a therapeutic means. Great progress in nano- and microengineered electrode platforms^[1–5] and ion delivery techniques^[6] for electrically communicating with neurons has enabled bioelectronic therapeutic

applications.^[9,11,12] Silicon photodiodes, which interconvert optical and electrical pulses, are reasonably efficient and mature technology at the crux of modern civilization that greatly benefits from extensive industrial infrastructure and know-how. Therefore, silicon-based devices were extensively studied for

Dr. D. Rand, G. Lubin, M. David-Pur, Prof. Y. Hanein
Tel Aviv University Center for Nanoscience and Nanotechnology,
and School of Electrical Engineering
Tel Aviv University
55 Haim Levanon St., Tel Aviv 699780, Israel
E-mail: yaelha@tauex.tau.ac.il


M. Jakešová, Dr. V. Đerek, Dr. E. D. Głowacki
Laboratory of Organic Electronics
Department of Science and Technology
Linköpings Universitet
Bredgatan 33, 60174 Norrköping, Sweden
E-mail: eric.glowacki@liu.se

I. Vėbraitė
Faculty of Agriculture
Food and Environment
Hebrew University of Jerusalem
POB 12, Rehovot 76100, Israel

Dr. V. Đerek
Center of Excellence for Advanced Materials and Sensing Devices
Ruđer Bošković Institute
Bijenička cesta 54, 10000 Zagreb, Croatia

Dr. T. Cramer
Department of Physics and Astronomy
University of Bologna
Viale Berti Pichat 6/2, I-40127 Bologna, Italy

Prof. N. S. Sariciftci
Linz Institute for Organic Solar Cells (LIOS)
Johannes Kepler University
Altenbergerstrasse 69, A-4040 Linz, Austria

 The ORCID identification number(s) for the author(s) of this article can be found under <https://doi.org/10.1002/adma.201707292>.

DOI: 10.1002/adma.201707292

neuronal stimulation applications and in particular for artificial retinal devices, some of which are in clinical trials or already on the market.^[12] Despite these clear advantages, silicon-based devices are not ideally suited to interface with soft and often very sensitive biological tissues. These devices are optimized to work in dry conditions, and electrical interconnects as well as many semiconductor materials corrode in a physiological setting, necessitating tightly sealed passivation and encapsulation. Moreover, these devices are hard and rigid, and create difficulties from mechanical mismatching, such as scar tissue formation.^[13–15] Silicon, as an indirect bandgap semiconductor, has a low absorbance coefficient, and therefore thickness of tens to hundreds of micrometers of silicon is necessary to absorb light efficiently, which sets a high lower-limit for the device thickness, further contributing to the overall rigidity, size, and relatively high weight.

Indeed, the motivation for finding novel materials with better properties for optical stimulation of cells was the focus of several recent studies involving organic semiconducting polymers,^[10,16,17] semiconducting nanocrystals,^[18–21] and amorphous silicon.^[22] Organic semiconducting polymers have shown the ability to photostimulate neurons^[16] and explanted retinas,^[10,17] and there is evidence that implanted films can impart light sensitivity to blind retinas *in vivo*.^[23] Semiconducting nanocrystals have also been successfully deployed for retinal stimulation.^[24] These systems boast ease of fabrication as well as flexibility, the ability to operate in a wet environment without extensive passivation/encapsulation, and biocompatibility. However, the stimulating mechanism underlying the observations of these new systems is often not fully elucidated, or the effects are primarily photothermal in nature. For example, photogenerated charge density values are too low ($<1 \mu\text{C cm}^{-2}$)^[25] to substantiate capacitive/electrical stimulation. Semiconducting polymer and inorganic nanocrystal systems can stimulate explanted retinas, however only delayed or latent responses are recorded.^[10,17,24] These observations have been rationalized by the slow (tens to hundreds of milliseconds) photocharging kinetics of these devices. Studies on the organic semiconductor-mediated electrophysiology of both excitable and nonexcitable cells suggest photothermal^[21,26–28] or thermocapacitive effects^[22,29] as dominant mechanisms in either depolarization or hyperpolarization of cells, rather than photocapacitive electrical stimulation.^[22,26] Though photothermal effects are appropriate for certain applications, direct electrical stimulation with short latency and high temporal resolution is required for most *in vivo* devices, especially chronic implants. Further, to avoid unwanted redox effects that may cause irreversible damage to cells as well as degradation of the device, electrical stimulation has to be truly capacitive in nature.^[30,31] There is a general consensus that capacitive coupling is the most safe and effective photostimulation mechanism.^[31,32] Thus, a fundamental requirement in designing photosensitive systems for neuronal stimulation is a high conversion efficiency of light into a capacitive displacement current sufficient for cell depolarization. Such a device should be biocompatible and ideally simple to fabricate in a scalable way with as small as possible dimensions and weight.

These requirements are the starting point for this work. Here we report on an efficient nanoscale semiconducting optoelectronic system optimized for neuronal stimulation:

the organic electrolytic photocapacitor. The devices comprise a thin (80 nm) tri-layer of metal and p–n semiconducting organic nanocrystals. When illuminated in physiological solution, these metal–semiconductor devices charge up, transducing light pulses into localized displacement currents that are strong enough to electrically stimulate neurons with safe light intensities, one hundred times below the safe ocular limit at 660 nm. The devices are freestanding, requiring no wiring or external bias, and are stable in physiological conditions. The semiconductor layers are made using ubiquitous and non-toxic commercial pigments via simple and scalable deposition techniques. We describe how, in physiological media, photovoltage and charging behavior depend on device geometry. To test cell viability and capability of neural stimulation, we show photostimulation of primary neurons cultured for three weeks on photocapacitor films. Finally, we demonstrate the efficacy of the device by achieving direct optoelectronic stimulation of light-insensitive retinal extracts in a similar manner to stimulation by current injection, proving the potential of this novel device platform for retinal implant technologies and for stimulation of electrogenic tissues in general. These results substantiate the conclusion that these devices are the first non-Si optoelectronic platform capable of sufficiently large photovoltages and displacement currents to enable a true capacitive stimulation of excitable cells.

The electrolytic photocapacitor we introduce here is a photodiode which produces electrical double layers upon illumination in water (Figure 1a). We hypothesized that the electrical potential difference induced in the surrounding electrolyte could affect the membrane potential of cells in the vicinity, even stimulating action potentials in excitable cells providing the voltage perturbation is large enough. The photocapacitors consist of a p–n heterojunction bilayer on top of a metallic back-contact. A surrounding physiological electrolyte is in contact with both the bottom metal and the top of the p–n junction (Figure 1a–c). Devices are fabricated by sequential physical vapor deposition through stencil masks, allowing control over geometries and compatibility with various substrates. For the photosensitive semiconductor p–n materials, we focused on hydrogen-bonded crystalline pigments owing to their favorable semiconducting properties combined with outstanding stability.^[33] The pigments used in this work are exploited industrially for high performance outdoor paints, printing inks, and cosmetics.^[34,35] In contrast to many semiconductor materials that are sensitive to water, hydrogen-bonded pigments are exceedingly stable in aqueous environments: they can be readily biofunctionalized using simple water-based chemistry^[36] and have recently been shown to be stable photoelectrocatalysts in a pH range from 1 to 12.^[37] The materials combination which emerged as most promising and was used throughout this study comprises a Cr/Au layer (2 nm/18 nm) followed by a 30 nm layer of metal-free phthalocyanine (H_2Pc) and 30 nm layer of *N,N'*-dimethyl perylene-3,4:9,10-tetracarboxylic diimide, PTCDI for short (Figure 1a,b). In an aqueous electrolyte, the device band diagram (shown at the beginning of the light pulse in Figure 1c) is that of a p–n donor–acceptor photodiode with the metal and the electrolyte forming the bottom and upper electrodes. Photogenerated excitons separate into free carriers at the donor–acceptor (p–n) interface.

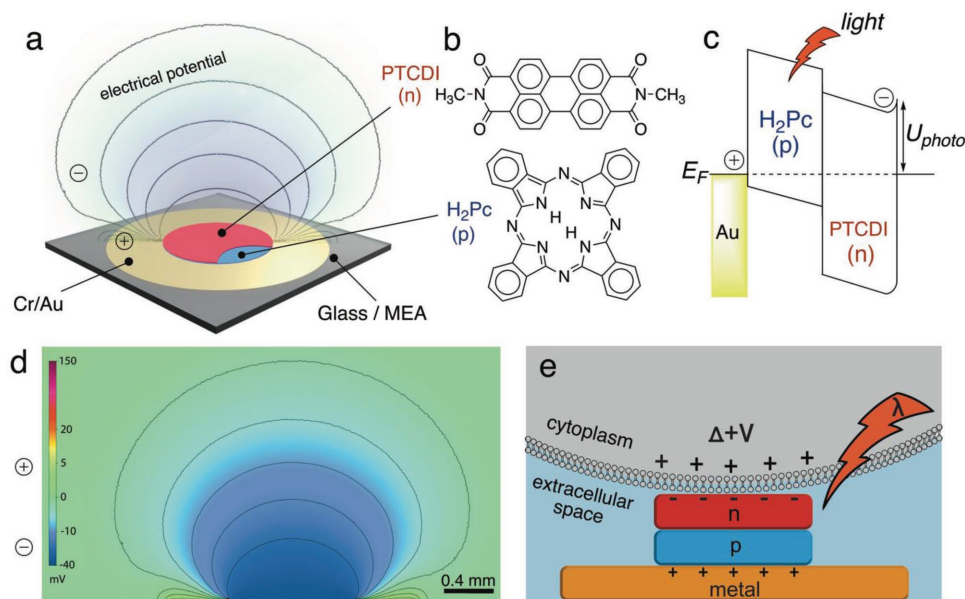


Figure 1. Organic photocapacitor devices. a) Schematic of the photocapacitor consisting of sequentially deposited Cr/Au and H₂Pc (p-type) and PTCDI (n-type). b) Molecular structures of the pigment semiconductors. Metal-free phthalocyanine (H₂Pc) functions as the primary light-absorbing layer and p-type electron donor, while *N,N'*-dimethyl perylenetetracarboxylic diimide (PTCDI) acts as the n-type electron-acceptor, which attains a negatively-charged surface upon illumination. c) Energy band illustration of a metal–p–n photocapacitor during the start of the illumination pulse when the capacitor charges. d) 2D slice of an electrostatic simulation of electrical potential distribution in electrolytic solution above a metal–p–n photocapacitor, at the point when the p–n junction charges to 250 mV. The positive potential is closely localized on the exposed metal film, while a negative potential “plume” extends from the top of the p–n layer. e) Mechanism of capacitive coupling of an illuminated photocapacitor with an adjacent cell.

The electrons accumulate in the n-type semiconducting layer and give rise to an oppositely charged double layer at the semiconductor–liquid interface. Photogenerated holes are injected into the metal and form an electrical double-layer with the surrounding electrolyte. The maximum possible photovoltage (U_{photo}) is given by the difference between the quasi-Fermi level at equilibrium and the conduction band edge of the n-type material. To understand the electrical potential in the surrounding aqueous environment, it is convenient to use electrostatic models. We calculated the charge and potential distribution for different charging voltages. The resultant distribution of electrical potential around a concentric photocapacitor device is plotted in Figure 1d. Perturbation of the potential has a magnitude of several tens of millivolts at tens of micrometers above the surface of the p–n layer. Therefore, the photo-induced voltage, which a cell in close contact with the photocapacitor will “feel”, can in principle be large enough to directly induce action potential generation via the capacitive coupling mechanism, as shown in Figure 1e. The choice of p–n, as opposed to n–p, gives a negative surface potential on the top of the organic layer, thereby leading to depolarization, as opposed to hyperpolarization, of the attached cell membrane. A further critical aspect of successful device design is the surface morphology of the p–n layer. Nanoscale structure allows for higher photocharge densities to be achieved. Our previous work with cell attachment on similar organic pigments showed that nanoscale roughening in the range of tens of nanometres played a key role in forming close interfaces with cells and cell attachment,^[21] which is in-line with other findings of nanomaterial/cell interfaces.^[38] Scanning electron microscopy revealed that 60 nm-thick p–n layers have a rough

truncated nanopillar-like morphology (Figure S1, Supporting Information) with relatively high surface area.

For photocapacitor characterization, we first fabricated 1.5×1.5 cm metallized (Cr/Au) glass slides with 1 cm^2 square p–n layer (denoted as type I samples). This arrangement was used to establish baseline parameters for photovoltage/photocurrent, spectral response, and stability. The gold electrode was wired (i.e., grounded) directly to the measurement equipment or floating in the electrolyte (Figure 2a). The spectral responsivity for photocathodic current was measured for wired samples, showing strong photocapacitive current generation in the red region of the visible spectrum, 700–600 nm, correlating closely with optical absorbance of the p–n stack (Figure 2b). Figure 2c shows photovoltage (V , trace 1) and photocurrent (I , trace 2) values of the photocapacitors measured between the Cr/Au layer versus reference electrode (Ag/AgCl) immersed in the solution, using pulsed illumination (5 ms, 660 nm). These results provide benchmark values for the photovoltages that the bilayer device can generate—around 280 mV (Figure 2c, trace 1). Corresponding displacement current values, I , are $400 \mu\text{A cm}^{-2}$ for light intensities of 60 mW cm^{-2} (Figure 2c, trace 2). The photocurrent profile has a capacitive transient shape, and by integrating charge of cathodic (charging) and anodic (discharging) phases, we obtain an equal value of charge, evidencing that the current is non-Faradaic in nature. We obtained more details on Type I devices using electrochemical impedance spectroscopy (EIS). In the dark, the p–n junction response is described by a geometric capacitance of 79.4 nF cm^{-2} that corresponds well to the layer thickness of the depleted n-type semiconductor ($d = \epsilon\epsilon_0 / C_g = 33 \text{ nm}$ with $\epsilon = 3$). Under illumination (620 nm , 0.81 mW cm^{-2}) the impedance drops as carriers

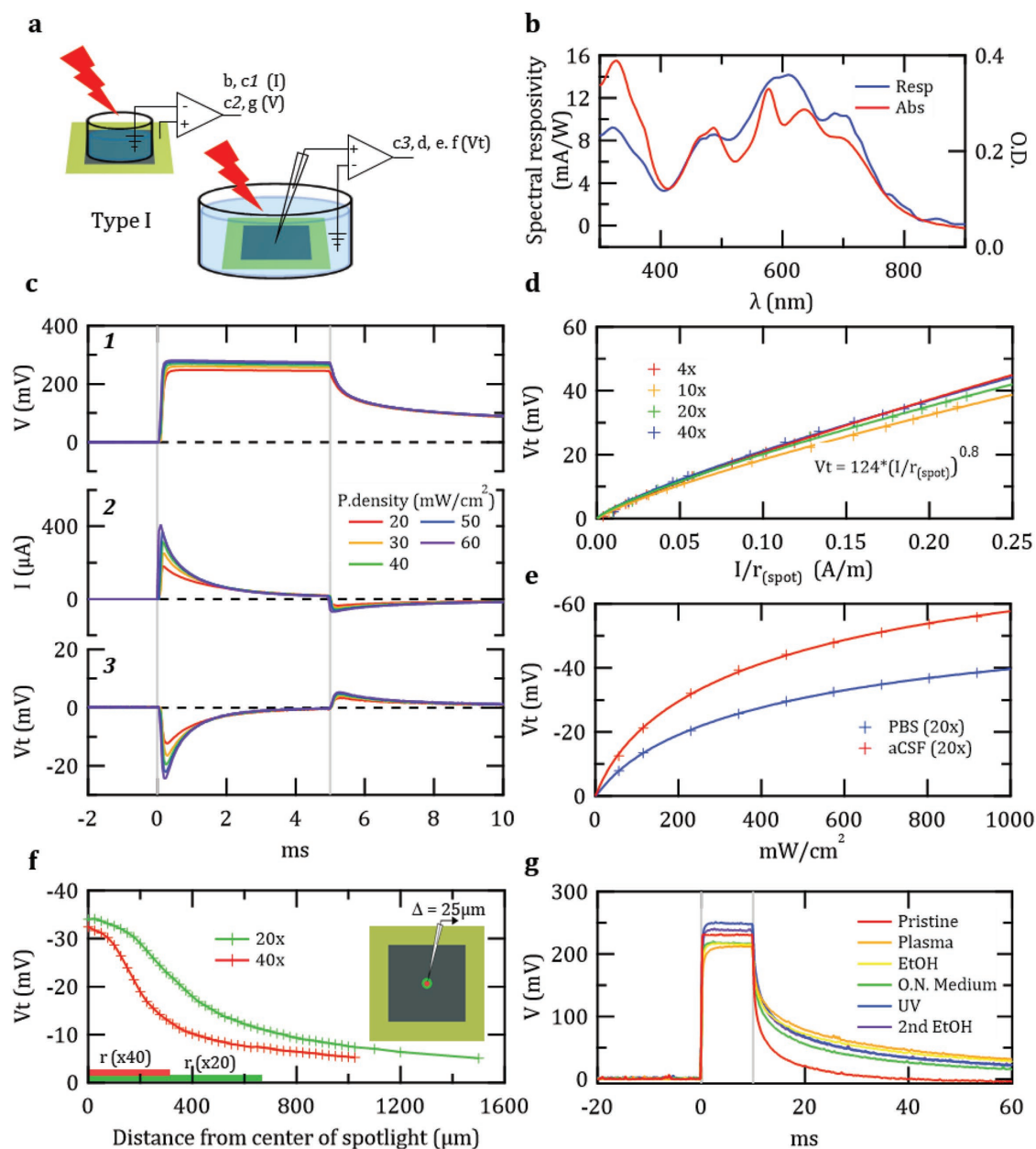


Figure 2. Photocapacitive charging of Cr/Au/H₂Pc/PTCDI film type I. a) Two photocapacitor measurement configurations for Type I samples (1 × 1 cm² p–n area on a 1.5 × 1.5 cm² gold coated glass slide): Grounded metal samples for voltage (V) and current (I) measurements, and “floating samples” for voltage transient (V_t) measurements. Numbers denote which figure panels show measurements in the given configuration. b) Optical absorbance overlaid with spectral responsivity of Type I photocapacitors. c) Photoelectric characterization. c1 and c2 are photovoltage (V) and photocurrent (I), respectively, measured between the bath electrode and the grounded p–n–metal device. c3 is the photovoltage transient (V_t) measured 10 μm above the p–n film, using a glass capillary electrode versus bath reference electrode. Vertical gray lines indicate onset and termination of the light pulses. The V_t follows the same dynamics as the capacitor charging current. d) Cathodic peak value of V_t (cpV_t) is a function of peak anodic current divided by the spot size radius r_(spot). e) cpV_t as a function of illumination intensity for two different electrolytes: phosphate-buffered saline and artificial cerebrospinal fluid. f) Lateral profile of cpV_t measured 10 μm above the surface for two different light spots that are significantly smaller than the p–n region. Measurements start from the center of the light spot and are measured laterally at 25 μm increments. Cathodic charging is strongest in the center of the spot, with V_t rapidly decaying outside of the directly illuminated region. g) Stress test results on grounded samples to evaluate the effects of different sterilization procedures. Measurement was done after sequential: oxygen plasma, triple treatment with absolute ethanol, storing overnight in buffer, UV sterilization, and second triple treatment with absolute ethanol.

are accumulated in the semiconducting layers. The EIS data allow us, on the basis of an equivalent circuit model (Figure S2, Supporting Information), to extract the capacitance between the

p–n layer and water ($C_{dl} = 3.8 \mu\text{F cm}^{-2}$) and the internal resistance of the illuminated p–n junction ($R_{int} = 1.2 \text{ k}\Omega \text{ cm}^{-2}$). The resistance in the dark, meanwhile, is very high ($\text{G}\Omega \text{ cm}^{-2}$) since

both p and n materials are intrinsic semiconductors. Photo-faradaic processes that follow a purely resistive path through the junction have only a very small contribution in the impedance spectra and show charge-transfer resistances in darkness or under illumination of $R_{CT} > 1.1 \text{ M}\Omega \text{ cm}^{-2}$, evidencing that the photocurrent is indeed capacitive in nature.

We next evaluated the photovoltage buildup created in solution above the photocapacitor, we define this parameter as the transient voltage, V_t . This is measured with a glass micropipette electrode in solution mounted on a micromanipulator. All measurements were taken with the micropipette tip $10 \mu\text{m}$ above the pigment surface, versus a large Ag/AgCl bath reference electrode, to give a realistic impression of what voltage perturbations cells adhered to the devices will encounter (Figure 2c, trace 3). These V_t measurements are taken without the Cr/Au metal film being electrically grounded, the metal is instead in a direct contact with an electrolyte, allowing us to characterize the operation of the photocapacitors in a wireless, free-standing mode. This scenario reflects the working conditions of a standalone implantable device. The measured electrical potential is in the order of a few millivolts, up to 25 mV (to be contrasted with 280 mV under the same illumination conditions when measuring the grounded sample - Figure 2c, trace 1). V_t profile and intensity is positively correlated with current profile (Figure 2c, trace 2). We found that cathodic peak values of V_t (cpV_t) are a function of peak anodic current divided by the spot size radius, r_{spot} , consistent with classic electrostatics for potential above a disk of charge (Figure 2d). Thus, while a displacement current can be readily associated with a known injected charge value, V_t can also be associated with a corresponding charge value. To empirically link between V_t and electrophysiology-relevant charge injection values we recorded V_t as a function of distance (0–30 μm) from a standard TiN MEA electrode, during stimulation with known current values (using values above the critical threshold needed to achieve action potential stimulation in explanted retinas, $\approx 0.1 \text{ mC cm}^{-2}$),^[25] (Figure S3, Supporting Information). We then repeated the same experiment, this time recording the transient photogenerated potentials at $10 \mu\text{m}$ above the pigment as a function of light intensity, using 10 ms pulses. Photovoltage values were recorded in both phosphate-buffered saline (PBS) and artificial cerebrospinal fluid (aCSF), which mimics the electrolytic environment in the eye. The peak values (cathodic phase) are plotted in Figure 2e, which shows that photovoltages suitable for direct retinal stimulation can be generated already with illumination values around 100 mW cm^{-2} . We found that measuring type I samples while illuminating a limited area (through $\times 20$ and $\times 40$ objective), the photocathodic voltage is highest in the middle of the illumination spot and decays rapidly at the edges of the spotlight (Figure 2e). The lack of lateral “leakage current” in the semiconductor layer is due to its intrinsic nature. We know from impedance analysis that the resistance of the layer in the dark is in the gigaohm range.

For proper operation in electrophysiological applications, devices must be stable in aqueous environments and compatible with sterilization procedures. We measured samples over several days in PBS solution without noting decrease of recorded photovoltage. Accelerated stress test involving sequential treatment with oxygen plasma, ethanol, incubation in cell

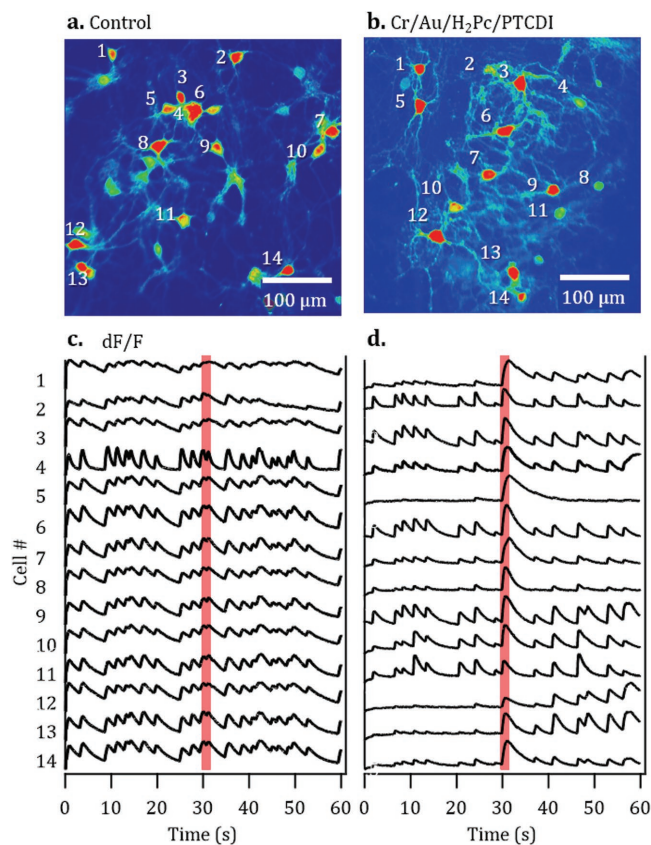


Figure 3. Photostimulation of neuronal cultures. a) Cortical primary neurons cultured on PDL-coated Petri dishes, control sample ($n = 4$). b) Cortical primary neurons cultured on type I devices ($n = 3$). c) Calcium imaging traces (dF/F) of neurons cultured on PDL-coated Petri dish. d) Ca imaging traces of neurons cultured on type I devices. Vertical red lines in (c) and (d) indicate a light stimulation of 100 consecutive pulses (600 nm, 480 mW cm^{-2} , pulse duration 5 ms, interpulse interval 10 ms).

culture medium, followed by UV sterilization treatment, and repeated ethanol rinsing, were performed to validate device stability (Figure 2g). In this study, we fabricated also devices from the well-known metal-containing phthalocyanine derivatives with copper and zinc, CuPc and ZnPc. These performed initially at a similar level as H₂Pc devices, however these devices were not stable with respect to delamination and failed during these stress-test experiments (Figure S4, Supporting Information). The Cr/Au/H₂Pc/PTCDI device configuration routinely passed the entire stress test sequence without significant loss in photovoltage or visible delamination.

Having established details on the relationships between device structure and photovoltage behavior, we proceeded to demonstrate stimulation of primary neuronal cultures (Figure 3). We compared dissociated mice cortical neurons cultured on type I sample (Cr/Au/H₂Pc/PTCDI, $n = 3$) with neurons cultured on standard Petri dishes coated with poly-D-lysine (PDL – a standard cell adhesion layer, $n = 3$). After 4 d in vitro (DIV) we infected the cultures with a viral vector for expressing the calcium indicator GCaMP6 and imaged neural activity at DIV 14. All cultures on both types of substrates developed into viable neural networks, exhibiting spontaneous

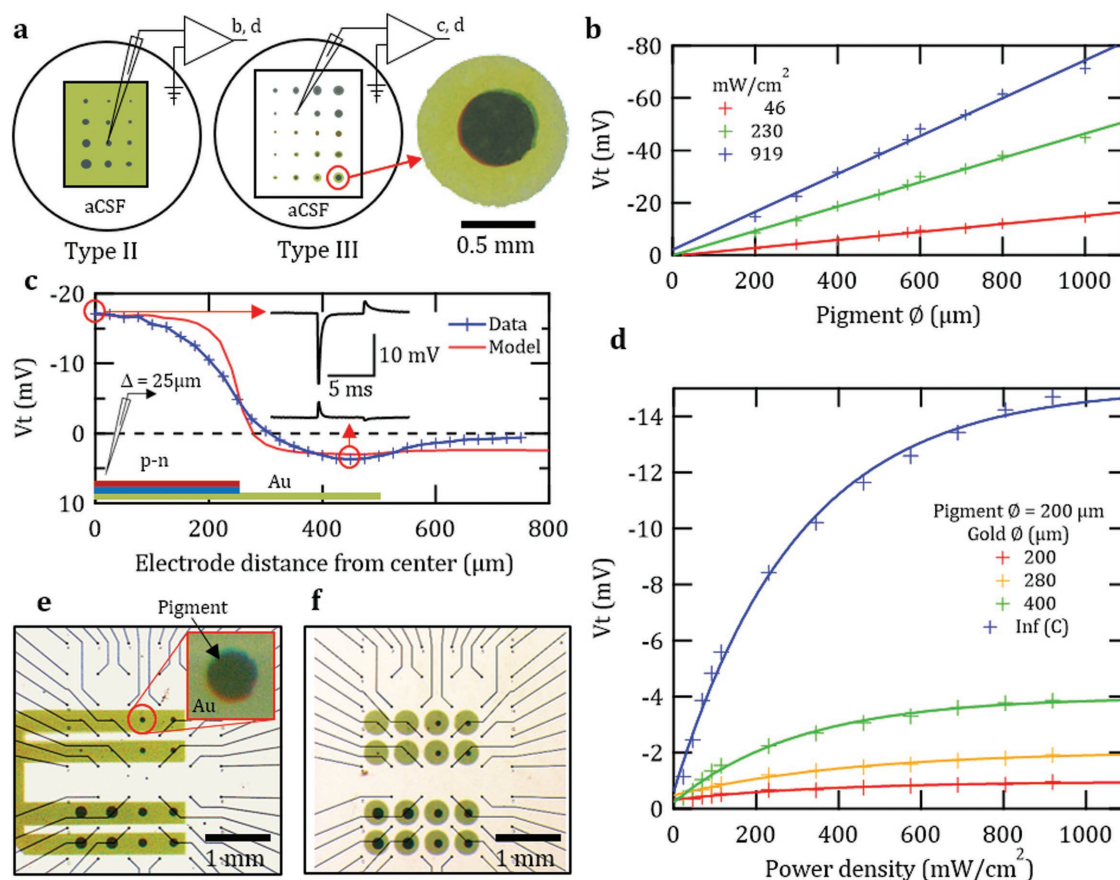


Figure 4. From films to pixels. a) Type II samples comprise p–n circular islands of varying size deposited on an “infinitely large” gold layer. Type III are devices where the size of both p–n islands and the underlying metal is varied. b) The effect of p–n island size. Cathodic peak values of voltage transients (cpV_t) from type II samples as a function of p–n island size for three different illumination intensities. V_t is measured $10 \mu\text{m}$ above the center of the p–n islands. Light spot size is larger than the maximal island size. c) Lateral cpV_t profile measured $10 \mu\text{m}$ above a type III sample, showing the maximum value of V_t in the center of the p–n island, with voltage changing sign above the metal film. Measurements are from the center of the p–n island and moving aside at $25 \mu\text{m}$ increments. d) The effect of gold size on V_t measured $10 \mu\text{m}$ above the p–n film in type III samples with constant p–n island size and variable metal size. e, f) p–n circular islands of varying size deposited in between the electrodes of multielectrode arrays with either “infinitely large” (e) or $\varnothing = 480 \mu\text{m}$ of circular (f) gold layer.

activity as indicated by the fluorescent calcium imaging (Figure 3a,b). Using a pulsed light stimulation, composed of 100 pulses of 600 nm, 480 mW cm^{-2} , 5 ms pulse duration, 10 ms inter-pulse interval, we were able to detect a clear response only in a neuronal network that was cultured on type I device samples (Figure 3d). A video of the experiment shown here is provided as Video S1 in the Supporting Information. It is important to note that the kinetics of the calcium indicators are relatively slow and do not show reliable single action-potential-associated calcium signals.^[39] Therefore, only a burst of activity that results from a train of pulses can accumulate into a detectable signal. In order to evidence the photocapacitive mechanism behind the observed action potential generation, we evaluated the contribution of photothermal heating (Figure S5, Supporting Information). We utilized a calibrated pipette conductometric technique^[40] to measure local heating at the p–n device surface. Using the same illumination protocol, with the pulse train of 5 ms pulses, we registered temperature increases of $0.28 \text{ }^\circ\text{C}$ over the timescale of 1.5 s. The magnitude of these temperature changes indicates that a photothermal effect cannot be

responsible for the action potential generation observed in these neuronal cultures. These calcium imaging studies show the potential of the organic photocapacitors to stimulate action potentials and the stability of the devices in physiological environment, and furnish preliminary evidence that the materials are not detrimental to cell viability.

While larger uniform films are appropriate for stimulating neurons, patterned pixels offer several possible advantages including integration with recording electrode arrays and stimulation localization. Decrease in the lateral dimensions of the device is also required for effective retinal implants or other applications requiring electrical stimulation. To design devices for effective stimulation using isolated islands, samples with p–n areas of different sizes, ranging from 200 to 1000 μm in diameter, on top of a large, (type II), or finite (type III) gold surface area were fabricated and their V_t was measured as described before (Figure 4a). We evaluated the dependence of cathodic photovoltage as a function of the sizes of both the p–n junction area and the underlying gold layer. First, we varied the size of p–n junction islands on a gold film that had

100-fold greater area than the p–n regions, which we refer to as the “infinite” gold condition (Figure 4a, device type II). We found that photocathodic voltage scales linearly with p–n junction diameter, and that p–n junction diameter of less than 150 μm is unlikely to yield effective stimulation (Figure 4b). By laterally scanning the micropipette electrode from the center of the p–n junction all the way to the exposed gold layer, it becomes clear that the sign of the recorded potential shifts from negative on top of the p–n junction to positive over the metal, and remains positive to around 250 μm away from the edge of the p–n layer (Figure 4c). The measured potential in solution closely follows the electrostatic model, plotted together with experimental data, for potential in the vicinity of disks of charge. To quantify the effect of exposed gold on performance, the p–n junction diameter was held constant 200 μm and we varied the underlying gold size (Figure 4a, device type III). It is apparent that the gold in contact with surrounding electrolyte is necessary for accommodating the positive charges photogenerated by the p–n junction. An increased area of exposed gold is a critical parameter to obtain higher photocathodic values (Figure 4d). Using these findings, we modified commercial multielectrode arrays (MEAs) with p–n pixels on large gold traces (Figure 4e) and on 470 μm diameter gold disks (Figure 4f), creating platforms for localized photostimulation and simultaneous neural recording.

The embryonic chick retina is a well-established model for the development of the visual system^[41] and the retina in particular.^[42] At embryonic day 14 (E14), retinal cells are in an early maturation stage,^[43,44] but the retina is not yet sensitive to light. Opsins mRNA only begins to appear in a small region by then,^[45] while photoreceptor electrical activity in response to light is not detected before E17.^[41] Thus, at this stage of development, the chick retina serves as a light insensitive retinal mode.^[24]

Retinas (E14) were placed on type II or type III device-modified MEAs (Figure 5a). Outer nuclear layer (Figure 5b) and the nerve fibre layer (Figure 5c) are readily apparent in visual inspection with a light microscope. The intrinsic light-insensitivity is always verified prior to further experiment, though E14 seldom show any light sensitivity. To provide an internal control, we used a single MEA electrode in the mode of typical electrical stimulation,^[25] delivering 8 μA over 300 μs , generating a direct action-potential response in the retina (Figure 5d). We find that the exact same direct responses are generated synchronously in ganglion cells and fibers at the vicinity of the illuminated photocapacitor device pixels by delivering a 2 ms light pulse through the objective (Figure 5e). In the chick retina, direct responses are easily recognized as they propagate in both directions along the nerve fibers (retrograde and anterograde). We have previously shown that these responses result from direct activation of ganglion cells, they can be suppressed by the presence of voltage-gated sodium channels blocker, tetrodotoxin,^[46] but not in the presence of synaptic transmission blockers.^[25] The latency of a direct response becomes larger when detected on electrodes that are further away from the stimulating electrode. Indeed, measured propagation direction (red and blue regression lines in Figure 5a) and speed of $0.33 \pm 0.045 \text{ m s}^{-1}$ (calculated from the latency of the response between two adjacent electrodes, 500 μm apart), correspond well with fiber layer alignment (Figure 5c) and known action potential propagation

speed in the chick retina.^[46] The photocapacitive pixels elicit the same direct response as current-injected MEA electrodes ($n = 4$ retinas), verifying that the devices are photocapacitively evoking direct retinal responses. Since these spikes are synchronized, they are summed into a large electrical signal that is superimposed on the stimulating signal. The amplitude of the recorded response is a function of the amount of recruited somas and nerve fibers that is directly correlated with the stimulus light intensity (Figure 5f). Both type II and type III MEA samples were found to evoke direct responses in retinas. Successful stimulations were made with all pixels of 100 μm diameter and above for pulse duration as short as 1 ms. The minimal intensities for detecting a response were 430 and 130 mW cm^{-2} for 100 and 200 μm diameter pixels, respectively. Our results unambiguously show deterministic and rapid action potential generation in light-insensitive retinas.

In this investigation we used ubiquitous organic semiconductor pigments with an extensive history: They have been used as photoconductors in xerographic applications^[47] since the 1960s, and indeed in the earliest heterojunction organic photovoltaic devices.^[48] Organic xerography is a direct inspiration for the physical concepts used in this work. The active materials we explored are cheap and nontoxic materials which constitute colorants used commercially in applications as various as printing inks, cosmetics, and automobile paints.^[34,35] We used these organic semiconductors to address several major challenges in the realm of optical stimulation of neuronal systems. Foremost is the ability to perform safe electrical stimulation mediated by a simple optoelectronic system. The devices we studied are free-standing (electrically floating structures) and are fabricated via scalable fabrication steps where the substrate remains at room temperature, which allows integration with arbitrary substrate materials. While silicon-based photodiodes have so far played a dominant role in the realm of artificial photoelectrical stimulation of neurons, silicon devices have several shortcomings compared with organic pigment layers. First, pigment films have a higher absorbance coefficient, allowing them to efficiently absorb light. At 660 nm, used in this work, the absorbance coefficient of vacuum-evaporated H_2Pc is $3 \times 10^5 \text{ cm}^{-1}$, while silicon is $2.58 \times 10^3 \text{ cm}^{-1}$. This difference allows making thinner photoactive films much less invasive, as the devices can have thicknesses that are much smaller than single cells. Our devices are 500 times thinner than the thinnest state-of-the-art silicon diodes for retinal implants. Moreover, in our design, one has a nanostructured semiconductor surface in direct contact with the electrolytic medium/biological sample, there is no voltage drop on a passivation layer or on conducting interconnects in between. Silicon photocapacitive devices charge metal electrodes—here we have the semiconductor surface itself serving as the primary charge-carrying electrode. Secondary metal electrodes must be employed in the case of silicon since it is not stable in physiological aqueous media. It must be carefully encapsulated, and interconnects passivated using $\text{SiO}_2/\text{Si}_3\text{N}_4$ layers, for example. The organic p–n layers can make direct contact with the physiological environment due to their durability. Organic crystalline pigments like phthalocyanine and perylene diimide are famously indestructible in terms of chemical and photochemical stability.^[35] Further, the nontoxicity of both phthalocyanines and perylene pigments is

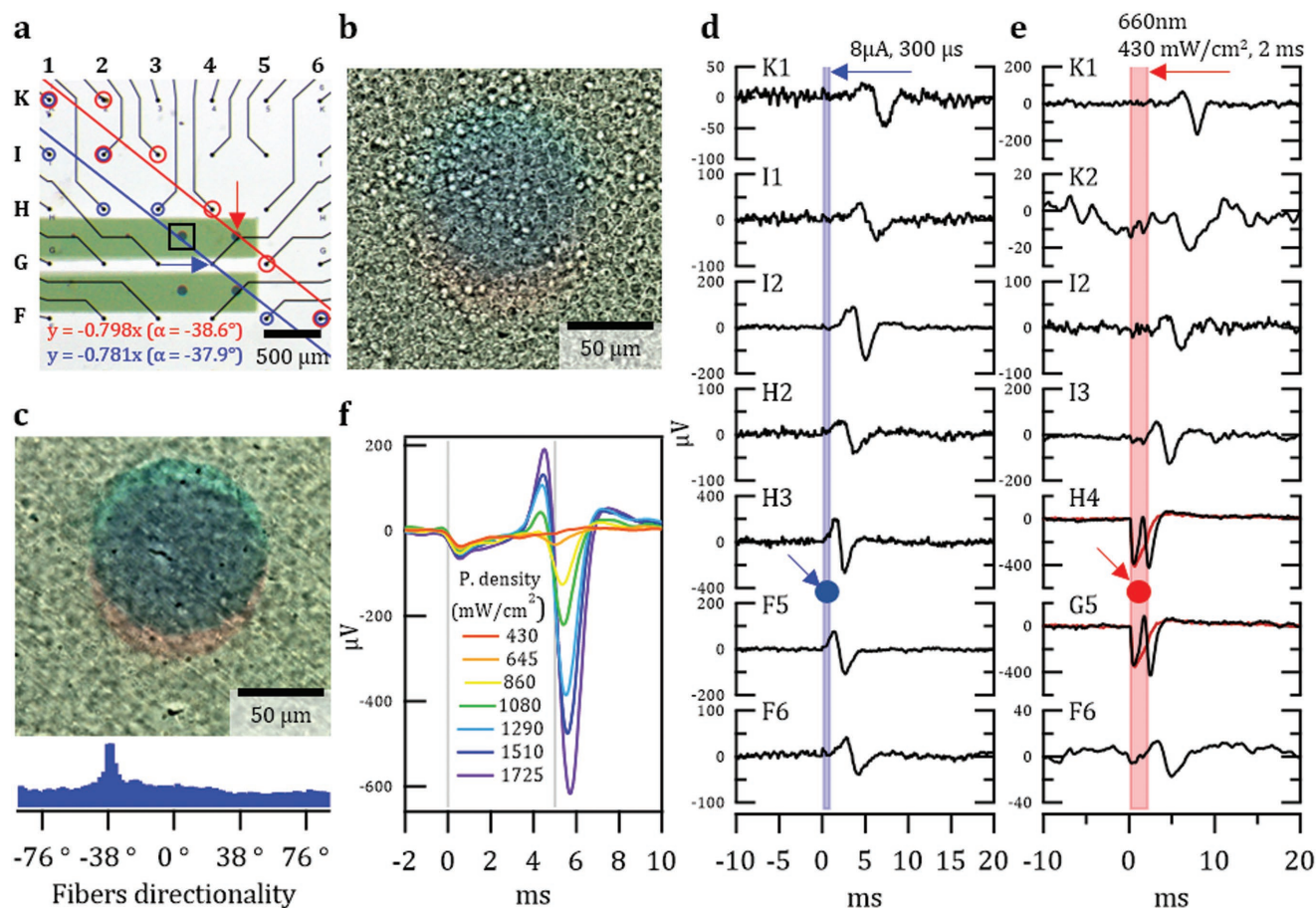


Figure 5. Direct responses of RGC in a light-insensitive retina. a) A piece of light insensitive embryonic chick retina was laid on the MEA shown in Figure 4e. Light pulses illuminated only a pigment bilayer of 100 μm marked by a red arrow using 40 \times objective. Electrical stimulation injected to electrode G4, marked by a blue arrow. Direct responses of the RGC were detected only in red-circled electrodes for light stimulation and blue-circled electrodes for electrical stimulation. Corresponding regression lines for these electrodes are shown and their linear equation, with a slope of 38°. b) An image of a retina placed on the MEA, with optical focus on the photoreceptor nuclear layer. The p-n island (marked with square in Figure 5a) is clearly visible beneath the retina. c) The same image as in (b) focused on the nerve fibre layer. The orientation of the fibers is clearly seen in the image, found to be 38° by the fast Fourier transform directionality histogram. d) Current pulse stimulation of the retina. Relative location of the injected electrode, G4, is marked by a blue arrow and circle. The latency of the response is increased when recorded from more distant electrodes to the stimulating electrode. The stimulating pulse is not detected in the recording due to the operation of the amplifier's blanking circuit. This measurement serves as an internal control. e) Photostimulation of the retina. Relative location of the illuminated pigment is marked by a red arrow and circle. Electrodes H4 and G5, which are close to the source, record the electrical signal generated by the photocapacitor device. This signal, which can also be recorded from pulses that did not evoke retinal responses, is plotted in overlaid red traces. f) Direct responses to 5 ms light pulse of different intensities showing the intensity-response dependence. Vertical gray lines indicate onset and termination of the light pulses.

well-documented.^[49] These materials are used in cosmetics, medical products, and tattoos. They are commercial colorants which belong to the lowest category of hazard and toxicity for consumer approved materials in the EU.

Achieving temporal control over neural stimulation requires activation with short latency of the response. In the case of retinal stimulation, such short latency responses are attributed to directly activating the retinal ganglion cells (RGCs). Direct activation of RGCs means that each stimulation pulse produces short latency synchronized action potentials in several somas and axons of RGCs that are located at the vicinity of stimulating electrode.^[25,50,51] In contrast, stimulation of neurons presynaptic to the ganglion cells results in the generation of bursts of unsynchronized spikes in the RGCs with much longer latency,

due to synapse transmission.^[52,53] Therefore, a major challenge in neuronal activation, in particular with photosensitive nanostructures, is to understand and to control the mechanism by which the activation is achieved, aiming for a sufficient charge injection for obtaining direct electrical activation similar to that of the best-optimized silicon-based electronics. Moreover, such electrical stimulation should be capacitive, which is considered safe and can be used for extended duration, unlike faradaic stimulation and thermal activation that are not considered optimal and should be avoided.^[31]

The photoelectric transduction of our device is sufficient to stimulate the RGC layer in a direct electrical manner at safe light intensities. In terms of neuronal stimulation benchmark parameters, our ultrathin organic device reaches parity with the

state-of-the-art silicon diode-based technologies. We are able to evoke action potentials in retinas using the same light intensity range as triple-tandem silicon retinal stimulation diodes.^[9,54] The range of pulsed light intensities and durations we have used has been deemed two orders of magnitude below the safe limit for ocular stimulation.^[9] Moreover, 660 nm is within the biological tissue transparency window, which can enable different *in vivo* applications.

To conclude, we demonstrated a new and advantageous concept to photostimulate neurons. Primary neurons were cultured on our photocapacitor devices for three weeks, demonstrating viability of both the devices and the cells. The latter could readily be photostimulated using short impulses of light. We next integrated photocapacitors onto commercial MEAs, enabling simultaneous photoexcitation and recording. Using this platform, we demonstrated effective direct photostimulation of light-insensitive embryonic chicken retinas. The MEA allows us to make an *in situ* control of conventional electrical stimulation, thereby we verify that the photocapacitor arrays and the electrical stimulation have the exact same retinal response. We experimentally discount the presence of photothermal heating effects. The culmination of this work is stand-alone photocapacitors with organic pixels of 100 μm in diameter to locally and reproducibly evoke action potentials. Future research of this device concept should involve optimizing materials to afford higher responsivity and photovoltage, allowing smaller pixels and lower light intensities. Different nano- and microstructuring of the organic material must be explored to yield optimal coupling with cells. The technology is a new platform that can interact with living cells via a true capacitive coupling mechanism, thus enabling safe and versatile next-generation implant technologies, and already at the level demonstrated here is suitable for various *in vivo* applications in peripheral or central nervous system stimulation, for example, in the context of traumatic injury. Success in these efforts requires deployment of the devices on implantable and/or bioresorbable substrates, and evaluation of their stability and performance *in vivo*.

Experimental Section

Materials: Phthalocyanine H₂Pc (Alfa Aesar), ZnPc (BASF), and CuPc (BASF) were each purified by threefold temperature gradient sublimation in a vacuum of $<1 \times 10^{-3}$ torr. PTCDI, *N,N'*-dimethyl-3,4,9,10-perylenetetracarboxylic diimide (BASF), was likewise purified thrice by sublimation.

Device Fabrication: Photocapacitor devices were fabricated using physical vapor deposition processes either on clean microscope slide glass or on commercial multielectrode arrays (Multichannel Systems GmbH), with both metal and organic regions defined by stainless steel shadow masks. Both glass and MEA substrates, after solvent cleaning, were treated with UV-generated ozone and a layer of chromium (2 nm) followed by gold (18 nm) was evaporated at a base pressure of $<1 \times 10^{-6}$ mbar at a rate of 0.2 and 3–5 \AA s^{-1} , respectively. From previous work,^[55] it is known that following these fabrication procedures gives primarily Cr₂O₃ rather than metallic Cr. Following evaporation, the samples were exposed to UV-generated ozone for 15 min and then placed into a chamber held at 75 °C containing vapor of *n*-octyltriethoxysilane (OTS) for 2 h. Following OTS treatment the substrates were rinsed with acetone and water and placed in boiling acetone for 15 min to remove multilayers and excess silanization physisorbed on the Cr/Au or TiN electrodes (the latter in the case of MEA). The OTS layer was found to

improve the adhesion of the organic semiconductor layer and prevent delamination, and produced reliably higher photovoltage than bare Cr/Au. Following rinsing with isopropanol and water and drying under a nitrogen stream, the samples were placed with appropriate shadow masking in an organic materials evaporator. The pigment layers were evaporated at a rate of 0.5 \AA s^{-1} for the p-type layer and 5–6 \AA s^{-1} for the n-type at a base pressure of $<1 \times 10^{-6}$ mbar, to give a total thickness of 60 nm consisting of 30 nm of p- and n-type.

Photoresponse Characterization: Photocurrent and photovoltage characterization were done on 1.5 \times 1.5 cm metallized (Cr/Au) glass slides with 1 cm² square p–n layer (type I sample). A glass chamber was placed on the p–n later coated area, leaving outside the exposed gold in the perimeter (left sample in Figure 2a). The chamber was filled with electrolyte, either PBS or modified Tyrode's solution (5 $\times 10^{-3}$ M KCl, 25 $\times 10^{-3}$ M NaHCO₃, 10 $\times 10^{-3}$ M glucose, 1.2 $\times 10^{-3}$ M MgSO₄, 1.2 $\times 10^{-3}$ M HEPES, 0.5 $\times 10^{-3}$ M glutamine, 2.5 $\times 10^{-3}$ M CaCl₂). A photogenerated response was measured between the underlying metal electrode and a reference electrode (either Au or Ag/AgCl) in the solution. The measurement unit consisted of a current amplifier (model 1212; DL Instruments) or voltage amplifier (model ELC-03XS, npi electronic GmbH). Photoresponse characterization was also done (for data in Figure 2g) on a simplified setup using a Techtronix TDS3000 oscilloscope, connecting the positive lead to the photocapacitor back electrode and the negative lead to a Ag/AgCl electrode immersed in electrolyte. Type I samples give large enough currents and voltages to be readily measured on an oscilloscope without any amplification. Measurement of voltage transients in electrolyte was done by immersing the entire samples of type I, II, or III in the electrolyte (right sample in Figure 2a for type I and Figure 4a for type II and III), and recording 10 μm above the surface using a micropipette electrode filled with 3M KCl, mounted on a computer motorized micromanipulator (model PatchStar, Scientifica) versus Ag/AgCl reference electrode in the electrolyte. The illumination unit, for all above experiments, consisted of a light-emitting diode with a peak wavelength of 660 nm (Thorlabs) mounted on an Olympus upright microscope (BX51WI) using a 4 \times or water immersion objectives of 10, 20, and 40 \times , resulting in illumination intensities within the range of 0.6–1725 mW cm⁻². A Xenon-Discharge Lamp and Czerny-Turner Monochromator were used as a light source to acquire the photocurrent spectra. The photocurrents were amplified using a Lock-in amplifier and chopper operated at 29 Hz. The current rms values were acquired as a function of wavelength and normalized for the light intensity as measured with a pyroelectric detector. Impedance spectra were acquired in 0.1 M KCl with a Metro-Ohm PGSTAT 204 at open-circuit potential conditions.

Electrostatic Modeling: Electric potential distribution of the device immersed in electrolyte was modeled using the Robin Hood Solver software package for complex 3D electrostatic problems using the Robin Hood calculation method.^[56] Charged photocapacitor devices were modeled as two concentric metal plates—larger bottom gold electrode fixed at 0 V potential, and the smaller top electrode which represented an equipotential surface at the top of the p–n junction, and which could be set at arbitrary potentials depending on the modeled electrode. The electrodes in the model were separated by a thin dielectric layer with relative permittivity of 3, characteristic to the organic semiconductors used here. The dielectric layer in the model represented the p–n junction region of the device. The space surrounding the device was modeled as a dielectric with relative permittivity of 80.1, representing a water-based electrolyte. All the dimensions in the model were true to the experimentally measured devices.

Neural Cultures: All mice were treated in accordance with the principles and procedures of the Israel National Institute of Health and the United States National Institutes of Health Guidelines for the Care and Use of Laboratory Animals. Protocols were approved by the Institutional Animal Care and Use Committee of the Tel Aviv University. Dissociated cortical cultures were prepared as follows: the entire cortices of SV129-mice, post-natal 0–1, were removed. Cortical tissue was digested with 0.065% trypsin (Biological Industries) in PBS for 15 min, followed by mechanical dissociation by trituration. Cells

were re-suspended in a modified essential medium without phenol red and glutamine, 5% horse serum, 50×10^{-3} M glutamine, 0.02×10^{-3} M glucose, 0.5% Pen-Strep, 2% B-27, and 0.75% glutamax (Gibco) and plated on either a poly-D-lysine (Sigma) covered Petri dish (control) or on type I samples (experiment) with a cell density of 3000 cells mm^{-2} ($\approx 700 \times 10^3$ cells per dish). Cultures were maintained at 37 °C with 5% CO_2 . Growth medium was partially replaced every 3–4 d. At 4 DIV, cultures were infected with AAV-CAG-GCaMP6s viral vector (prepared by the Tel Aviv University vector core facility).

Optical Recording via Calcium Imaging: Calcium imaging recordings were performed on 14 DIV in buffered mice artificial cerebrospinal solution (mice aCSF: 10×10^{-3} M HEPES, 4×10^{-3} M KCl, 1.5×10^{-3} M CaCl_2 , 0.75×10^{-3} M MgCl_2 , 139×10^{-3} M NaCl, 10×10^{-3} M D-glucose, adjusted with sucrose to an osmolarity of 325 mOsm, and with NaOH to a pH of 7.4). Images were acquired with an EMCCD camera (Andor Ixon-885) mounted on an Olympus upright microscope (BX51WI) using a 20 \times water immersion objective (Olympus, LUMPLFL NA 0.4). Fluorescent excitation was provided via a 120 W mercury lamp (EXFO x-cite 120 PC) coupled to a GFP filter cube (Chroma T495LP). Images were acquired at 59 fps in 2 \times 2 binning mode using Andor software data-acquisition card (SOLIS) installed on a personal computer, spooled to a high capacity hard drive and stored as uncompressed multipage tiff file libraries.

Electrical Recordings from Retinas: Direct retinal responses were recorded with 30 μm diameter TiN electrode MEAs. Coupling between the tissue and the electrodes was improved by placing a small piece of polyester membrane filter (5 μm pores; Sterlitech) and a ring weight on the retina. The filter was removed before light stimulation to minimize scattering. Retinas were kept at physiological conditions, at a temperature of 34 °C, and perfused (2–5 mL min^{-1}) with oxygenated (95% O_2 , 5% CO_2) chick aCSF solution (5×10^{-3} M KCl, 25×10^{-3} M NaHCO_3 , 9×10^{-3} M glucose, 1.2×10^{-3} M MgSO_4 , 1.2×10^{-3} M HEPES, 0.5×10^{-3} M glutamine, 2.5×10^{-3} M CaCl_2). Neuronal signals were amplified with MEA1060-UP amplifier with a built-in blanking circuit that ground the electrodes during current injection (gain \times 1100; MultiChannel Systems), digitized using a 64-channel analogue to digital converter (MC_Card; MultiChannel Systems), and recorded (MC_Rack; MultiChannel Systems). In vitro epi-retinal stimulation was carried out by injecting biphasic pulse of 300 μs to a single electrode of the MEA, using electrical stimuli generated by an external stimulator (STG4002; MultiChannel Systems) and a critical threshold for eliciting retinal responses of 0.4–1.4 mC cm^{-2} , similar to what has been reported in the literature, was found.

Supporting Information

Supporting Information is available from the Wiley Online Library or from the author.

Acknowledgements

No competing financial interests have been declared. The authors gratefully acknowledge the financial support from the Knut and Alice Wallenberg Foundation within the framework of the Wallenberg Centre for Molecular Medicine at Linköping University, the Austrian Science Fund FWF via the Wittgenstein Prize Solare Energie Umwandlung Z222-N19 for N.S.S., and the European Research Council under the European Community's Seventh Framework Program (FP7/2007-2013)/ERC grant agreement FUNMANIA-306707 for Y.H.. The authors thank Beatrice Fraboni for assistance with electrochemical impedance measurements, and Predrag Lazić for providing the electrostatic modelling software (Robin Hood Solver).

Conflict of Interest

The authors declare no conflict of interest.

Keywords

artificial retina, bioelectronics, neurostimulation, organic semiconductors

Received: December 14, 2017

Revised: March 4, 2018

Published online: May 2, 2018

- [1] N. A. Kotov, J. O. Winter, I. P. Clements, E. Jan, B. P. Timko, S. Campidelli, S. Pathak, A. Mazzatenta, C. M. Lieber, M. Prato, R. V. Bellamkonda, G. A. Silva, N. W. S. Kam, F. Patolsky, L. Ballerini, *Adv. Mater.* **2009**, *21*, 3970.
- [2] P. Fattahi, G. Yang, G. Kim, M. R. Abidian, *Adv. Mater.* **2014**, *26*, 1846.
- [3] R. Green, M. R. Abidian, *Adv. Mater.* **2015**, *27*, 7620.
- [4] M. H. Histed, V. Bonin, R. C. Reid, *Neuroendocrinology* **2009**, *63*, 508.
- [5] M. D. Ferro, N. A. Melosh, *Adv. Funct. Mater.* **2017**, *28*, 1704335.
- [6] D. T. Simon, E. O. Gabriellsson, K. Tybrandt, M. Berggren, *Chem. Rev.* **2016**, *116*, 13009.
- [7] S. H. Yun, S. J. J. Kwok, *Nat. Biomed. Eng.* **2017**, *1*, 1.
- [8] M. Scanziani, M. Häusser, *Nature* **2009**, *461*, 930.
- [9] K. Mathieson, J. Loudin, G. Goetz, P. Huie, L. Wang, T. I. Kamins, L. Galambos, R. Smith, J. S. Harris, A. Sher, D. Palanker, *Nat. Photonics* **2012**, *6*, 391.
- [10] D. Ghezzi, M. R. Antognazza, R. Maccarone, S. Bellani, E. Lanzarini, N. Martino, M. Mete, G. Pertile, S. Bisti, G. Lanzani, F. Benfenati, *Nat. Photonics* **2013**, *7*, 400.
- [11] E. Zrenner, K. U. Bartz-Schmidt, H. Benav, D. Besch, A. Bruckmann, V. Gabel, F. Gekeler, U. Grepplmaier, A. Harscher, S. Kibbel, J. Koch, A. Kusnyerik, T. Peters, K. Stingl, H. Sachs, A. Stett, P. Szurman, B. Wilhelm, R. Wilke, *Proc. R. Soc. B* **2011**, *278*, 1489.
- [12] A. T. Chuang, C. E. Margo, P. B. Greenberg, *Br. J. Ophthalmol.* **2014**, *98*, 852.
- [13] D. Prodanov, J. Delbeke, *Front. Neurosci.* **2016**, *10*, 11.
- [14] T. D. Y. Kozai, A. S. Jaquins-Gerstl, A. L. Vazquez, A. C. Michael, X. T. Cui, *ACS Chem. Neurosci.* **2015**, *6*, 48.
- [15] A. Butterwick, P. Huie, B. W. Jones, R. E. Marc, M. Marmor, D. Palanker, *Exp. Eye Res.* **2009**, *88*, 22.
- [16] D. Ghezzi, M. R. Antognazza, M. Dal Maschio, E. Lanzarini, F. Benfenati, G. Lanzani, *Nat. Commun.* **2011**, *2*, 166.
- [17] V. Gautam, D. Rand, Y. Hanein, K. S. Narayan, *Adv. Mater.* **2014**, *26*, 1751.
- [18] T. C. Pappas, W. M. S. Wickramanyake, E. Jan, M. Motamedi, M. Brodwick, N. A. Kotov, *Nano Lett.* **2007**, *7*, 513.
- [19] L. Bareket, N. Waiskopf, D. Rand, G. Lubin, M. David-Pur, J. Ben-Dov, S. Roy, C. Eleftheriou, E. Sernagor, O. Cheshnovsky, U. Banin, Y. Hanein, *Nano Lett.* **2014**, *14*, 6685.
- [20] M. Zangoli, F. Di Maria, E. Zucchetti, C. Bossio, M. R. Antognazza, G. Lanzani, R. Mazzaro, F. Corticelli, M. Baroncini, G. Barbarella, *Nanoscale* **2017**, *9*, 9202.
- [21] M. Sytnyk, M. Jakešová, M. Litviňuková, O. Mashkov, D. Kriegner, J. Stangl, J. Nebesářová, F. W. Fecher, W. Schöfberger, N. S. Sariciftci, R. Schindl, W. Heiss, E. D. Głowacki, *Nat. Commun.* **2017**, *8*, 91.
- [22] Y. Jiang, J. L. Carvalho-de-Souza, R. C. S. Wong, Z. Luo, D. Isheim, X. Zuo, A. W. Nicholls, I. W. Jung, J. Yue, D.-J. Liu, Y. Wang, V. De Andrade, X. Xiao, L. Navrazhnykh, D. E. Weiss, X. Wu, D. N. Seidman, F. Bezanilla, B. Tian, *Nat. Mater.* **2016**, *15*, 1023.
- [23] J. F. Maya-Vetencourt, D. Ghezzi, M. R. Antognazza, E. Colombo, M. Mete, P. Feyen, A. Desii, A. Buschiazzi, M. Di Paolo, S. Di Marco, F. Ticconi, L. Emionite, D. Shmal, C. Marini, I. Donelli, G. Freddi, R. Maccarone, S. Bisti, G. Sambuceti, G. Pertile, G. Lanzani, F. Benfenati, *Nat. Mater.* **2017**, *16*, 681.

- [24] L. Bareket-Keren, N. Waiskopf, D. Rand, G. Lubin, M. David-Pur, J. Ben-Dov, S. Roy, C. Eleftheriou, E. Sernagor, O. Cheshnovsky, U. Banin, Y. Hanein, L. Bareket, N. Waiskopf, D. Rand, G. Lubin, M. David-Pur, J. Ben-Dov, S. Roy, C. Eleftheriou, E. Sernagor, O. Cheshnovsky, U. Banin, Y. Hanein, *Nano Lett.* **2014**, *14*, 6685.
- [25] C. Sekirnjak, P. Hottoway, A. Sher, W. Dabrowski, A. M. Litke, E. J. Chichilnisky, *J. Neurophysiol.* **2006**, *95*, 3311.
- [26] N. Martino, P. Feyen, M. Porro, C. Bossio, E. Zucchetti, D. Ghezzi, F. Benfenati, G. Lanzani, M. R. Antognazza, *Sci. Rep.* **2015**, *5*, 8911.
- [27] Y. Lyu, C. Xie, S. A. Chechetka, E. Miyako, K. Pu, *J. Am. Chem. Soc.* **2016**, *138*, 9049.
- [28] F. Lodola, N. Martino, G. Tullii, G. Lanzani, M. R. Antognazza, *Sci. Rep.* **2017**, *7*, 1.
- [29] M. G. Shapiro, K. Homma, S. Villarreal, C.-P. Richter, F. Bezanilla, *Nat. Commun.* **2012**, *3*, 736.
- [30] I. Schoen, P. Fromherz, *J. Neurophysiol.* **2008**, *100*, 346.
- [31] S. F. Cogan, *Annu. Rev. Biomed. Eng.* **2008**, *10*, 275.
- [32] I. Schoen, P. Fromherz, *Biophys. J.* **2007**, *92*, 1096.
- [33] E. D. Głowacki, G. Voss, N. S. Sariciftci, *Adv. Mater.* **2013**, *25*, 6783.
- [34] H. Zollinger, *Color Chemistry. Syntheses, Properties and Applications of Organic Dyes and Pigments*, Wiley-VCH, Weinheim, Germany **2003**.
- [35] *High Performance Pigments* (Eds: E. B. Faulkner, R. J. Schwartz), Wiley-VCH, Weinheim, Germany **2009**.
- [36] E. D. Głowacki, R. R. Tangorra, H. Coskun, D. Farka, A. Operamolla, Y. Kanbur, F. Milano, L. Giotta, G. M. Farinola, N. S. Sariciftci, *J. Mater. Chem. C* **2015**, *3*, 6554.
- [37] M. Jakešová, D. H. Apaydin, M. Sytnyk, K. Oppelt, W. Heiss, N. S. Sariciftci, E. D. Głowacki, *Adv. Funct. Mater.* **2016**, *26*, 5248.
- [38] F. Santoro, S. Dasgupta, J. Schnitker, T. Auth, E. Neumann, G. Panaitov, G. Gompper, A. Offenhäusser, *ACS Nano* **2014**, *8*, 6713.
- [39] C. Grienberger, A. Konnerth, J. Wu, T. Teramoto, Y. F. Chang, M. Nakano, A. S. Abdelfattah, M. Fujiwara, T. Ishihara, T. Nagai, R. E. Campbell, *Neuroendocrinology* **2012**, *73*, 862.
- [40] J. Yao, B. Liu, F. Qin, *Biophys. J.* **2009**, *96*, 3611.
- [41] J. Mey, S. Thanos, *Brain Res. Rev.* **2000**, *32*, 343.
- [42] M. N. Vergara, M. V. Canto-Soler, *Neural Dev.* **2012**, *7*, 22.
- [43] C. Prada, J. Puga, L. Perez-Mendez, R. Lopez, G. Ramirez, *Eur. J. Neurosci.* **1991**, *3*, 559.
- [44] S. Doh, H. Hao, S. C. Loh, T. Patel, H. Y. Tawil, D. K. Chen, A. Pashkova, A. Shen, H. Wang, L. Cai, *BMC Dev. Biol.* **2010**, *10*, 8.
- [45] S. L. Bruhn, C. L. Cepko, *J. Neurosci.* **1996**, *16*, 1430.
- [46] D. Raz-Prag, G. Beit-Yaakov, Y. Hanein, *J. Neurosci. Methods* **2017**, *291*, 20.
- [47] D. S. Weiss, M. Abkowitz, *Chem. Rev.* **2010**, *110*, 479.
- [48] C. W. Tang, *Appl. Phys. Lett.* **1986**, *48*, 183.
- [49] K. Hunger, *Rev. Prog. Color. Relat. Top.* **2005**, *35*, 76.
- [50] D. Boinagrov, J. Loudin, D. Palanker, *J. Neurophysiol.* **2010**, *104*, 2236.
- [51] M. Eickenscheidt, M. Jenkner, R. Thewes, P. Fromherz, G. Zeck, *J. Neurophysiol.* **2012**, *107*, 2742.
- [52] A. Stett, W. Barth, S. Weiss, H. Haemmerle, E. Zrenner, *Vision Res.* **2000**, *40*, 1785.
- [53] D. Tsai, S. Chen, D. A. Protti, J. W. Morley, G. J. Suaning, N. H. Lovell, *PLoS One* **2012**, *7*, e53357.
- [54] L. Wang, K. Mathieson, T. I. Kamins, J. D. Loudin, L. Galambos, G. Goetz, A. Sher, Y. Mandel, P. Huie, D. Lavinsky, J. S. Harris, D. V. Palanker, *J. Neural. Eng.* **2012**, *9*, 46014.
- [55] M. Kaltenbrunner, G. Adam, E. D. Głowacki, M. Drack, R. Schwödiauer, L. Leonat, D. H. Apaydin, H. Groiss, M. C. Scharber, M. S. White, N. S. Sariciftci, S. Bauer, *Nat. Mater.* **2015**, *14*, 1032.
- [56] P. Lazič, H. Štefančič, H. Abraham, *J. Comput. Phys.* **2006**, *213*, 117.